Journal of Geophysical Research: Space Physics

Supporting Information for

Current Closure and Joule Heating in Data-Driven 3-D Auroral Arc Simulations

J. van Irsel[1], K. A. Lynch[1], A. Mule[1], M. D. Zettergren[2], J. K. Burchill[3], L. J. Lamarche[4], D. L. Hampton[5]

[1]Department of Physics and Astronomy, Dartmouth College, Hanover, NH, 03755 USA
[2]Physical Sciences Department, Embry-Riddle Aeronautical University, Daytona Beach, FL, 32114 USA
[3]Department of Physics and Astronomy, University of Calgary, Calgary, AB, T1N1N4 Canada
[4]SRI International, Menlo Park, CA, 94025 USA
[5]Geophysical Institute, University of Alaska Fairbanks, Fairbanks, AK, 99775 USA

Contents of this file

Introduction

Figures S1 – S4, along with Text S1 – S4, cover simulation comparisons that have been omitted from the main manuscript. They include descriptions and interpretations of their respective simulations, as well as top and side views, along with height-integrated Joule heating, of the two simulations in each comparison.

Figures S5 – S22 provide an isometric view, in addition to the top and side views given in their respective comparison figures, of each simulation covered in this work. The captions outline the simulation ID(s) the figure belong to, the combination of parameters, and the tube set ID. The combinations are encoded using SD, PF, and NB for SuperDARN, PFISR, and No Background, AM and UM for Accelerated and Unaccelerated Maxwellians, and AC, xA, xB, or xC referring to the combination of Swarm spacecraft. E.g. SD-UM-xA has a combination of SuperDARN derived background flow, the unaccelerated Maxwellian electron precipitation, and a FAC map replicated with only Swarm A.

Movie M1 can be found in Supporting Information along with this document. The caption of M1 can be found at the end of this document.

Text S1.

Comparison II, Figure S1, panels a – b, show the simulation results for the February 12 event with a SuperDARN derived background electric field of 8.6 mV/m directed 10° west of north (Simulation IIa). This is compared to the similarly strong, PFISR derived 11.9 mV/m in nearly the same direction (panels c – d, Simulation IIb). It is not surprising then, that there are few changes in current closure when comparing the two, as both have similar observations of $\bar{\mathbf{E}}$. One noteworthy difference is the amount of Hall current carried by the orange flux tubes. At 0.8 kA, the Simulation IIb flux tube carries around 33 – 35% more than its Simulation IIa counterpart. This is explained, in large part, by the roughly 38% increase in $|\bar{\mathbf{E}}|$. This same increase in electric field strength explains the 40 – 50% increase in height-integrated Joule heating, as shown in panels e and f, provided the $\mathbf{j} \cdot \mathbf{E} = \sigma_P |\mathbf{E}|^2$ relationship.

The red and green flux tubes for both simulations IIa – b show that the southern downward FAC sheet is not able to fully connect back to the magnetosphere inside this simulation volume. Most of the central upward FAC sheet accounts for the closure of just the northern edge of the primary return current sheet. The green flux tube, probing the bulk of this sheet, shows that around half closes upwards while the remaining 0.5 kA exits through the northern wall.

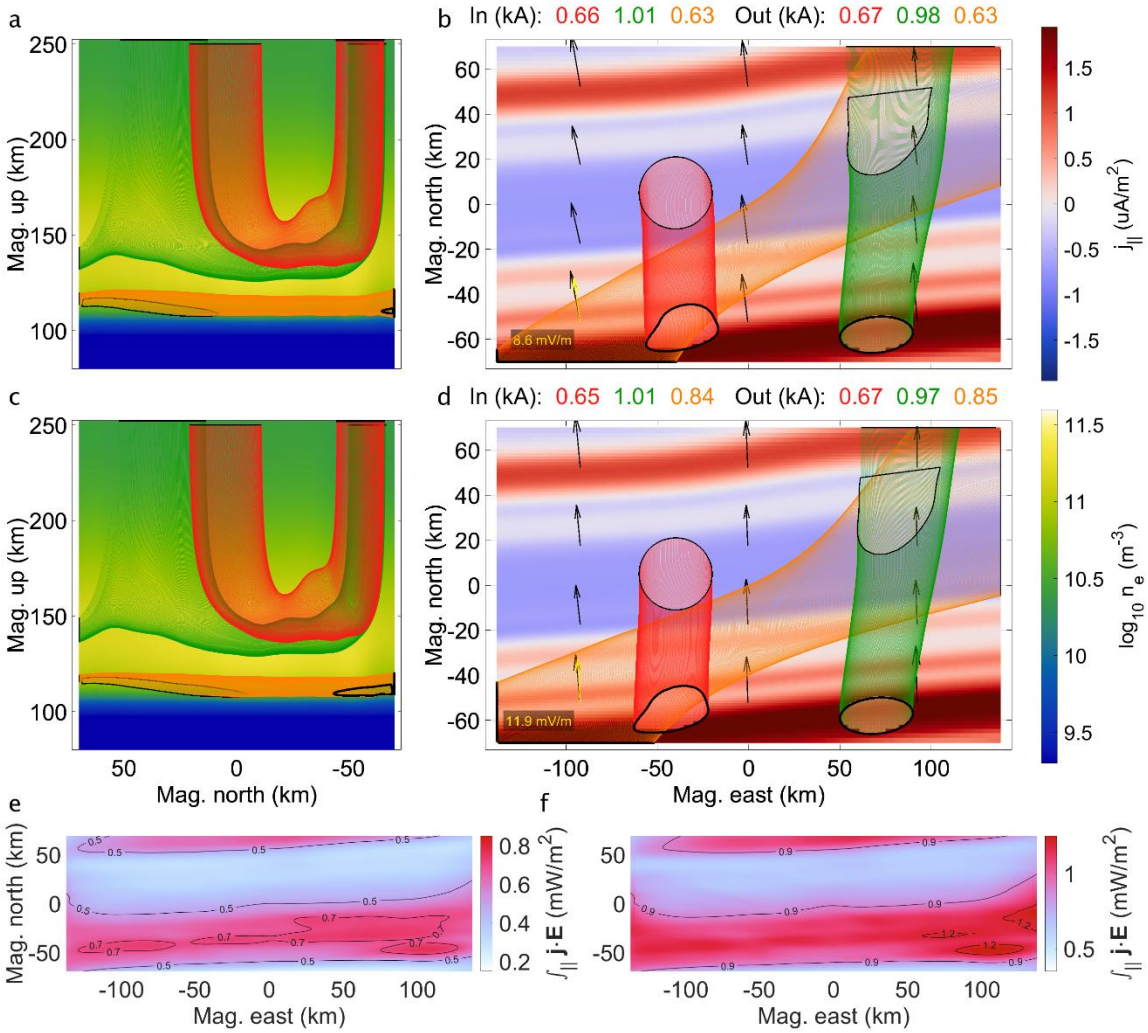

Figure S1. Comparison II (February 12, 10:22 UT): Top and side views of Simulation IIa with SuperDARN derived background flow (a, b) versus Simulation IIb with PFISR derived background flow (c, d) along with height-integrated Joule heating for Simulation IIa (e) and IIb (f). For plot details, see Section 2.8. Data sources: https://swarm-diss.eo.esa.int (Swarm), https://superdarn.ca/data-download (SuperDARN), https://data.amisr.com/database (PFISR), and https://rcweb.dartmouth.edu/LynchK (Simulation).

Text S2.

Comparison IV, Figure S2, is similar to Comparison II. Simulations IVa – b both have nearly northward background electric fields with 10.0 mV/m from SuperDARN and 21.0 mV/m from PFISR. Doubling the electric field strength increases the Hall current by a factor of around 2.8, depicted by the orange flux tube carrying 1.5 and 4.2 kA in simulations IVa – b respectively. One small difference between Comparisons II and IV is seen in the red flux tubes of Comparison IV, here carrying 1.3 kA: in Simulation IVa, the red flux tube requires just enough Hall current to rotate slightly to the east at its apex, while its Simulation IVb counterpart closes directly northward. As in Comparison II, again this doubling of the electric field strength nearly quadruples the height-integrated Joule heating, as seen in panels e and f.

The fact that our March 14 conjunction event has its precipitation collocated with downward FAC sheets, we argue, is consistent with both Simulations IVa – b. Given the sufficiently strong electric field strengths, the FAC closure depicted by the green and red flux tubes barely grazes the enhanced density/conductivity caused by the main arc precipitation. This suggests that this auroral arc system has a configuration that uncouples the FAC closure from the accelerated electron precipitation.

Both Comparisons II and IV outline that, in auroral arc systems with Pedersen conductivity sufficient for their FAC demands, FAC closure is less sensitive to the magnitude of the background electric field beyond some point. The Hall currents change mostly in amperage, linearly with the electric field strength, but less so in morphology.

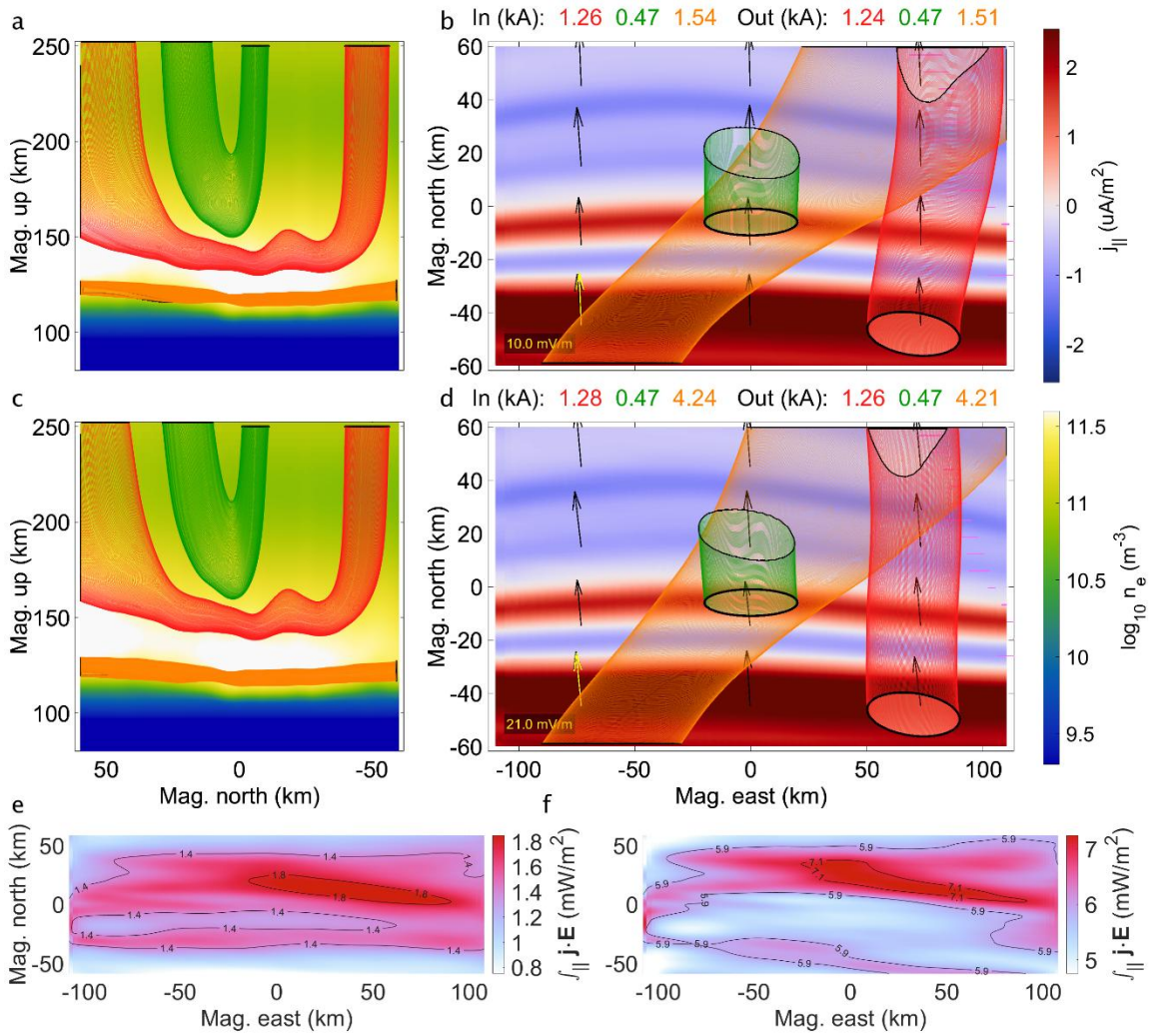

Figure S2. Comparison IV (March 14, 6:49 UT): Top and side views of Simulation IVa with SuperDARN derived background flow (a, b) versus Simulation IVb with PFISR derived background flow (c, d) along with height-integrated Joule heating for Simulation IVa (e) and IVb (f). For plot details, see Section 2.8. Data sources: https://swarm-diss.eo.esa.int (Swarm), https://superdarn.ca/data-download (SuperDARN), https://data.amisr.com/database (PFISR), and https://rcweb.dartmouth.edu/LynchK (Simulation).

Text S3.

Comparison VII shows a combination of a strong electric field and weak precipitation, in contrast to Comparison VI which shows a combination of a weak electric field and sufficiently energetic, low-reaching precipitation, and Comparison VIII with a very strong background electric field and the most energetic precipitation in our list of events.

Figure S3 shows the simulations from Comparison VII which both assume the nearly northward background electric field of 8.6 mV/m, as estimated by SuperDARN, like in Comparison II. This, combined with the weakest precipitations of our conjunction events—an energy flux of $Q_p = 2.3$ mW/m^2, acceleration potential of $U_a = 1.9$ keV, and characteristic energy of $E_0 = 1.4$ keV (see Figure 5 and Table 1)—renders this comparison relatively unaffected by the assumption of $\phi_u(E)$ over $\phi_a(E)$. The electron density in Simulation VIIb does drop lower by around 5 km, which adds a slight eastward drift to the green flux tube and provides around 0.6 kA more to the orange tube.

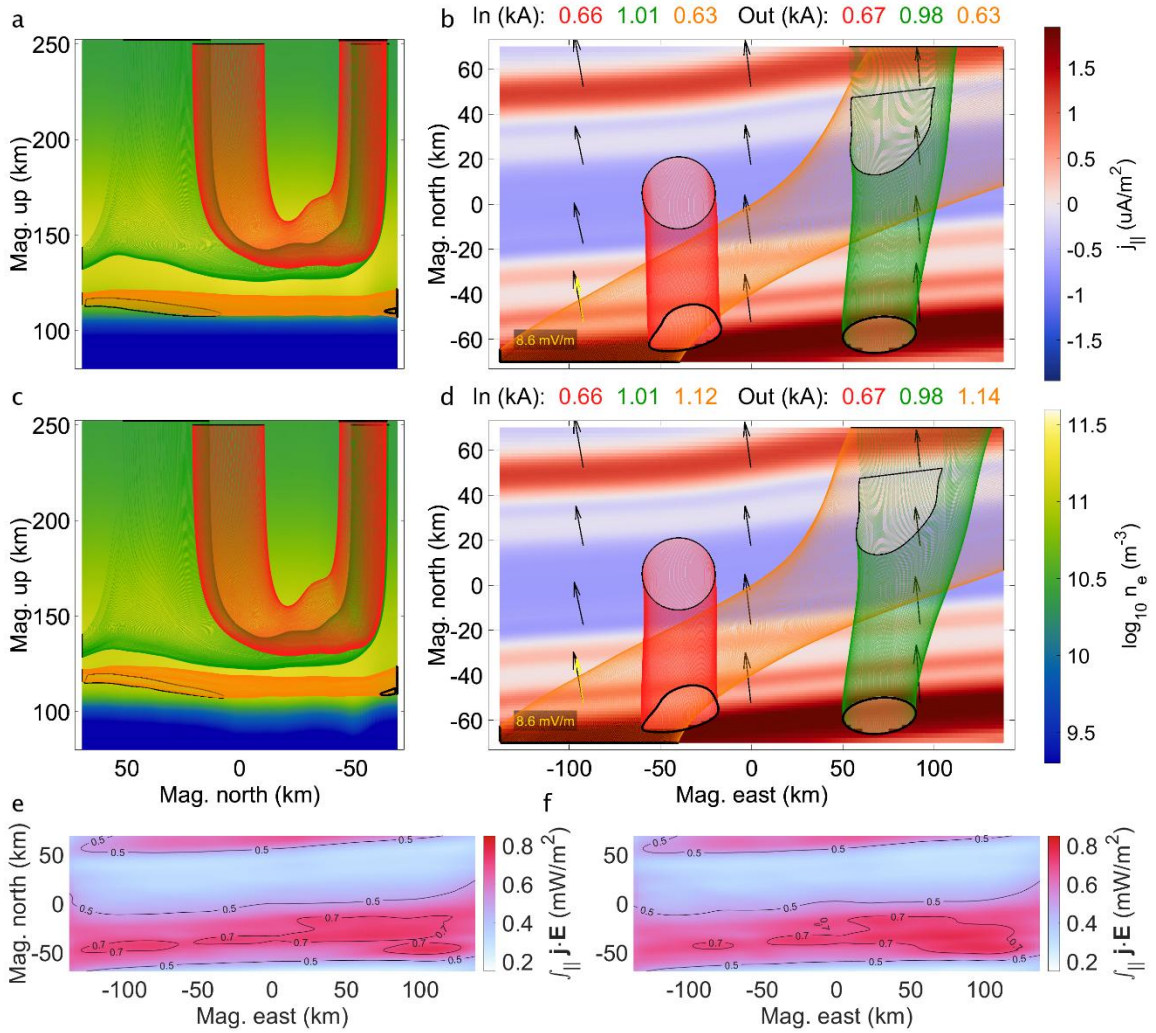

Figure S3. Comparison VII (February 12, 10:22 UT): Top and side views of Simulation VIIa with accelerated Maxwellian electron precipitation (a, b) versus Simulation VIIb with unaccelerated Maxwellian electron precipitation (c, d) along with height-integrated Joule heating for Simulation VIIa (e) and VIIb (f). For plot details, see Section 2.8. Data sources: https://swarm-diss.eo.esa.int (Swarm), https://superdarn.ca/data-download (SuperDARN), and https://rcweb.dartmouth.edu/LynchK (Simulation).

Text S4.

Figure S4 depicts Comparison IX. The flux tubes in both Simulations IXa – b all have rather agitated shapes, including the out-flux curves, due to the relatively noisy imagery pertaining to this event, which shows through the inverted energy flux depicted by Figure 5j. Regardless, the FAC, electric field strength, and precipitation parameters are all low, other than the source region characteristic energy, $T_s = 860$ eV (see Table 1). In terms of electron density enhancements, panels a and c show how a ratio of acceleration potential to source region characteristic energy of $U\_a/T\_s \approx 3.5$, compared to the previous ~ 7.5 in Simulation VIIIa, still does not match the affects from an unaccelerated $U\_s/T\_s = 1$ assumption to *E*-region densities.

Furthermore, the low FAC requirements, together with the wider spread of the precipitation energies, work in the favor of Pedersen closure, while the remaining parameters suggest a need for Hall closure. Ultimately, we see here that the $\phi_u(E)$ versus $\phi_a(E)$ assumption has a less pronounced effect on current closure morphology or the height-integrated Joule heating. The green current flux tube in Simulation IXb, albeit less dramatic, does stretch in the along-arc directions, perpendicular to $\mathbf{E}$, compared to Simulation IXa, suggesting increased amounts of Hall closure, but the orange nor red flux tubes vary greatly.

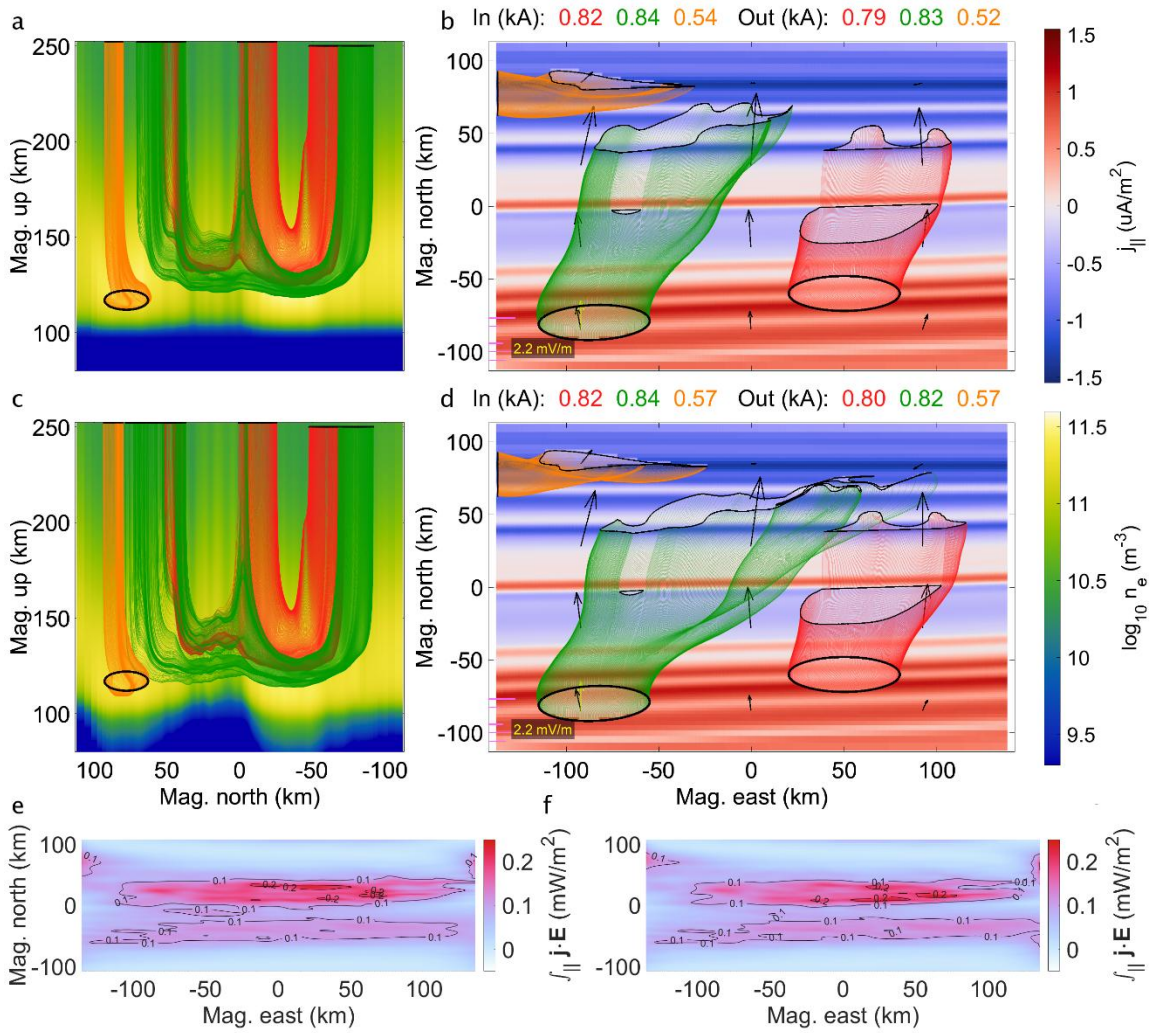

Figure S4. Comparison IX (March 4, 10:14 UT): Top and side views of Simulation IXa with accelerated Maxwellian electron precipitation (a, b) versus Simulation IXb with unaccelerated Maxwellian electron precipitation (c, d) along with height-integrated Joule heating for Simulation IXa (e) and IXb (f). For plot details, see Section 2.8. Data sources: https://swarm-diss.eo.esa.int (Swarm), https://superdarn.ca/data-download (SuperDARN), and https://rcweb.dartmouth.edu/LynchK (Simulation).

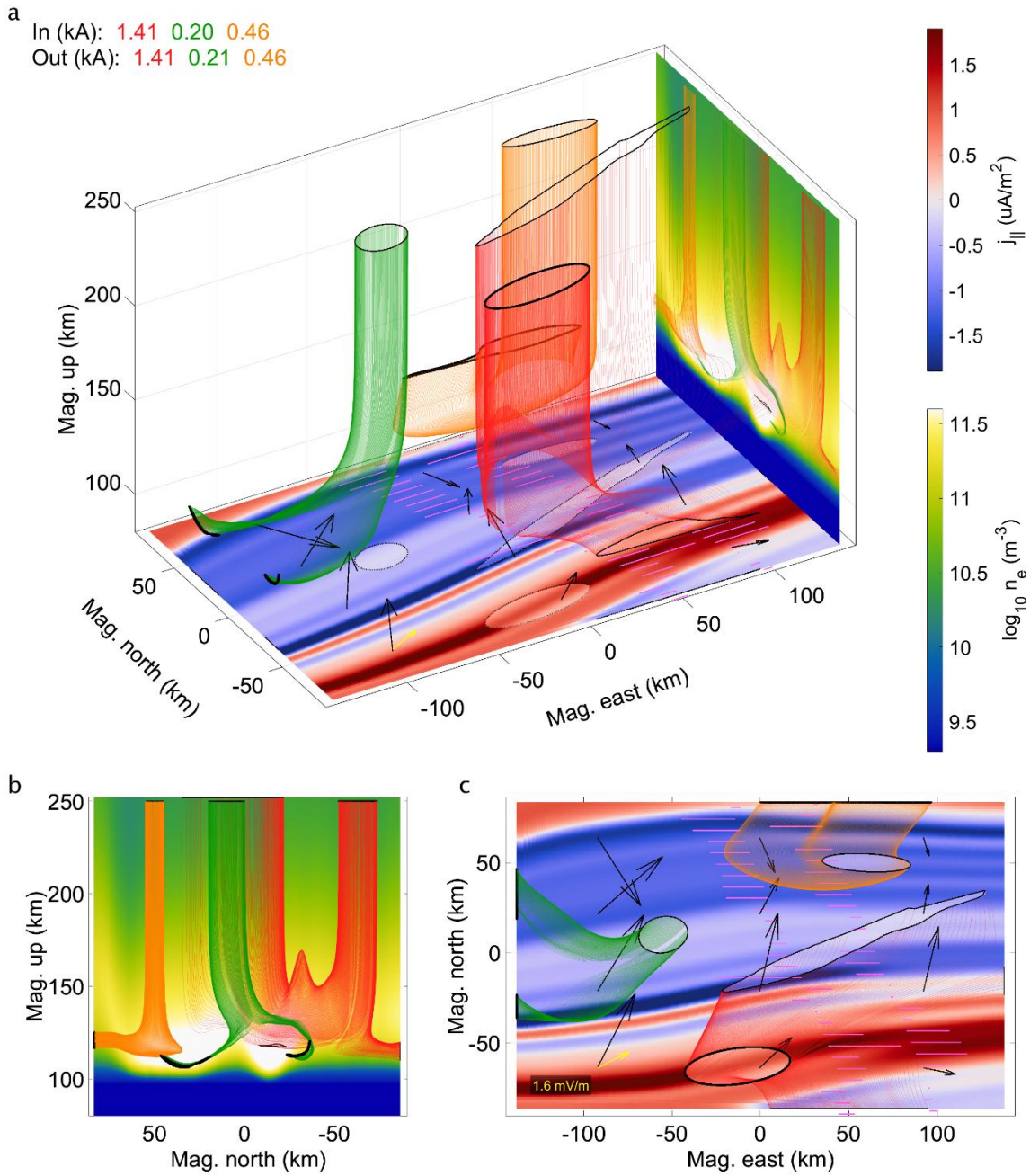

Figure S5. Simulations Ia, VIa, and Xa (February 10, 9:51 UT). Combination: SD-AM-AC. Tube set: 1. For plot details, see Section 2.8. Data sources found in respective comparison figures and the Open Research Section.

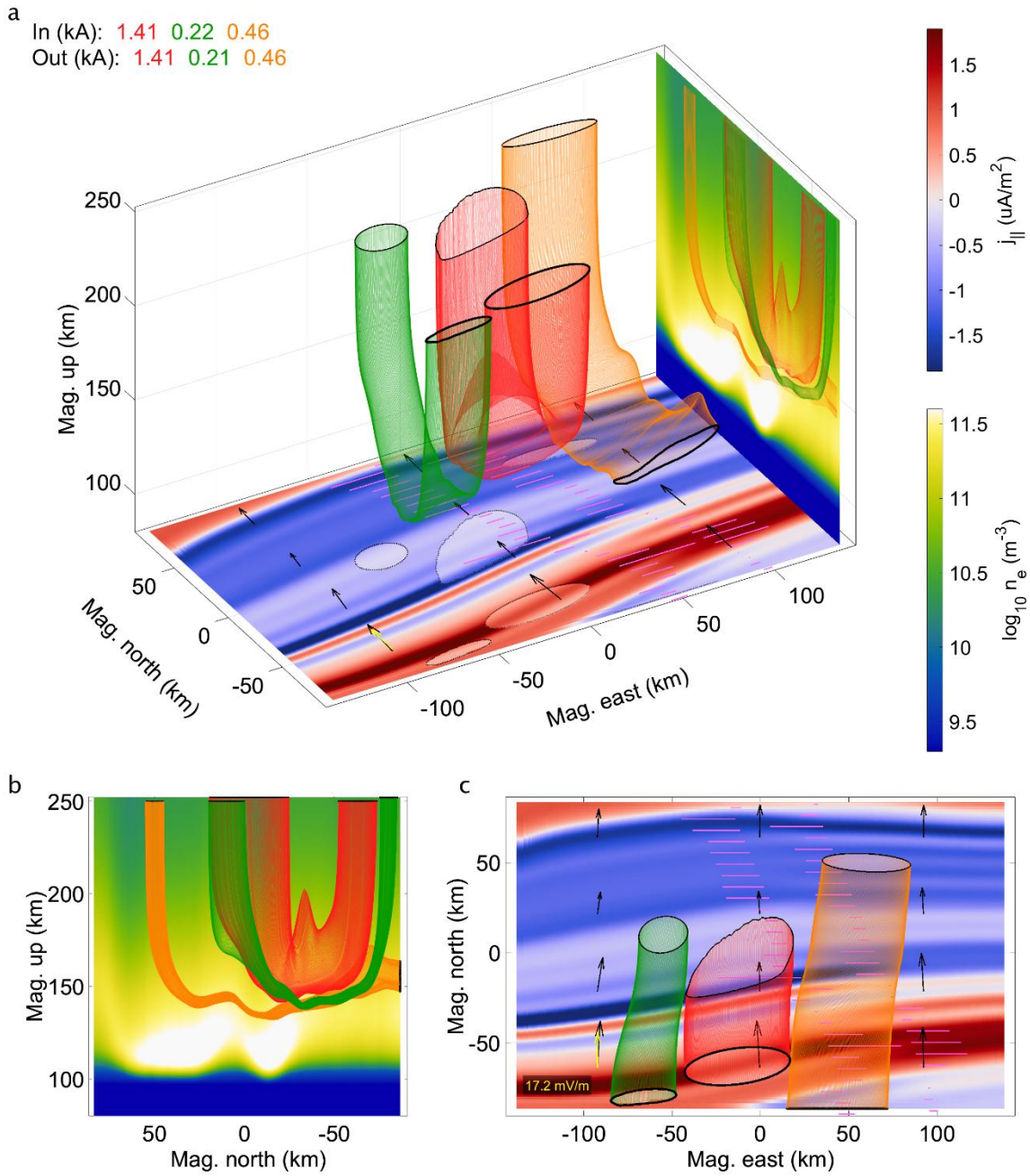

Figure S6. Simulation Ib (February 10, 9:51 UT). Combination: PF-AM-AC. Tube set: 1. For plot details, see Section 2.8. Data sources found in respective comparison figures and the Open Research Section.

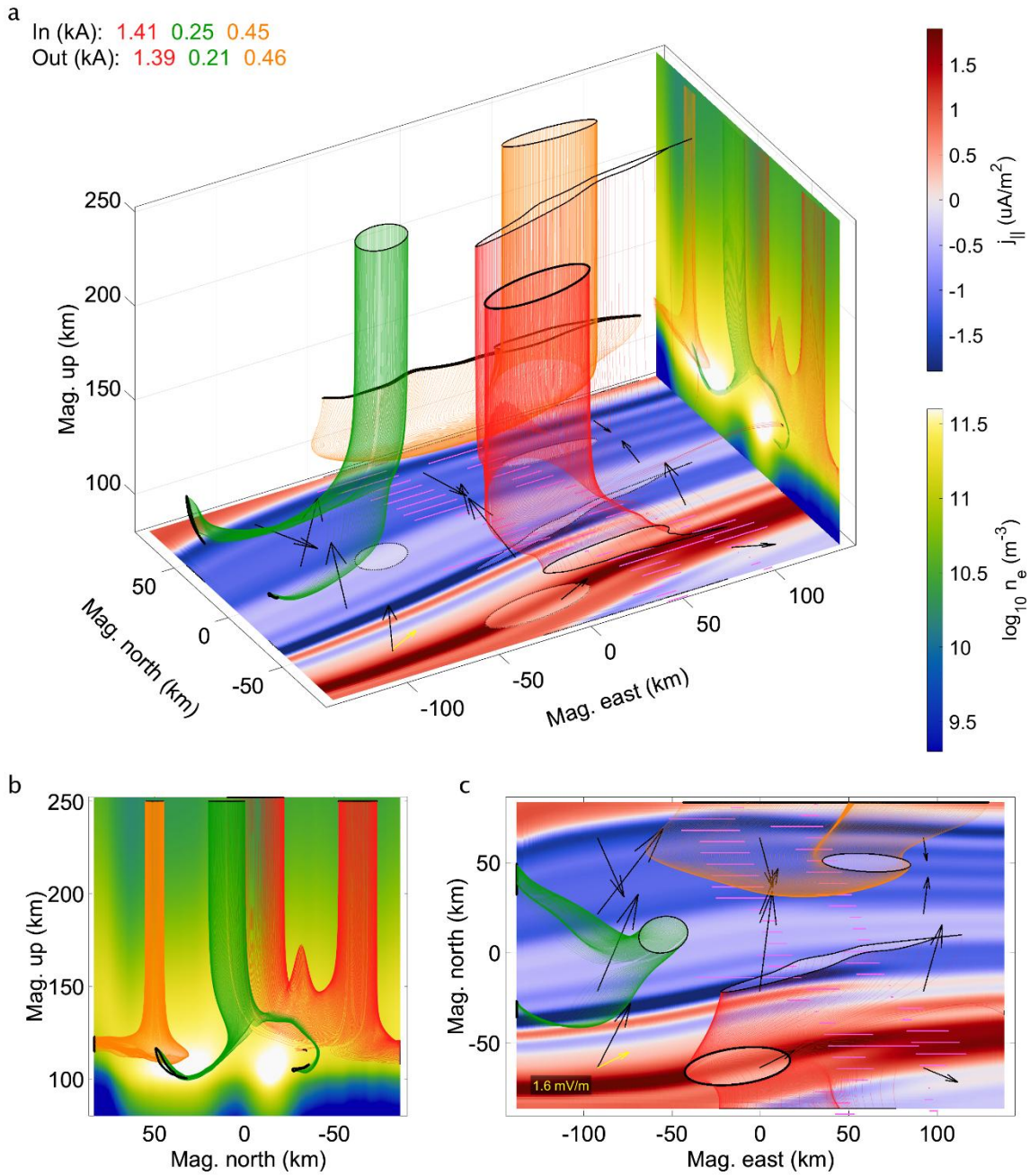

Figure S7. Simulation VIb (February 10, 9:51 UT). Combination: SD-UM-AC. Tube set: 1. For plot details, see Section 2.8. Data sources found in respective comparison figures and the Open Research Section.

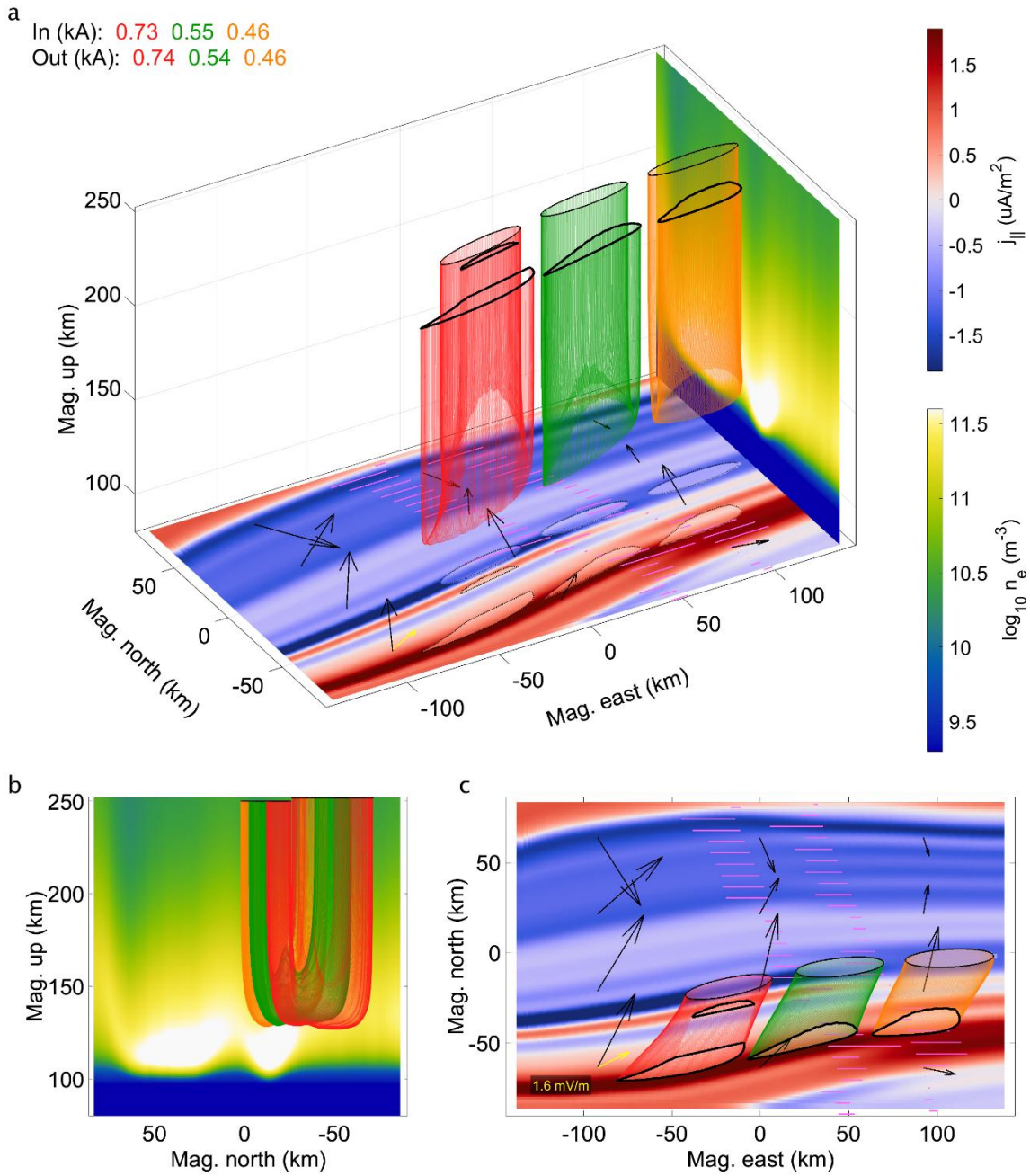

Figure S8. Simulations Ia, VIa, and Xa (February 10, 9:51 UT). Combination: SD-AM-AC. Tube set: 2. For plot details, see Section 2.8. Data sources found in respective comparison figures and the Open Research Section.

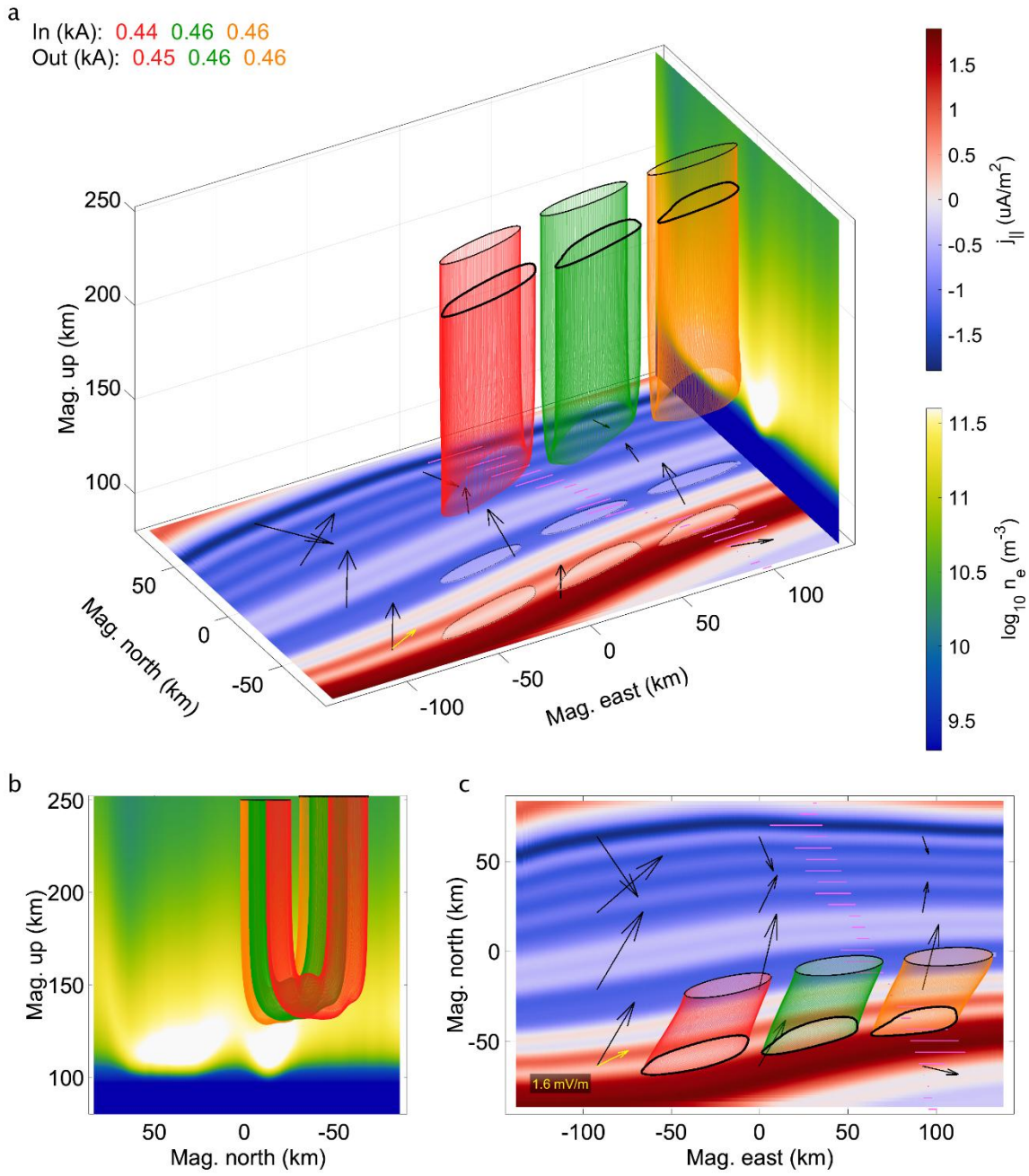

Figure S9. Simulation Xb (February 10, 9:51 UT). Combination: SD-AM-xA. Tube set: 2. For plot details, see Section 2.8. Data sources found in respective comparison figures and the Open Research Section.

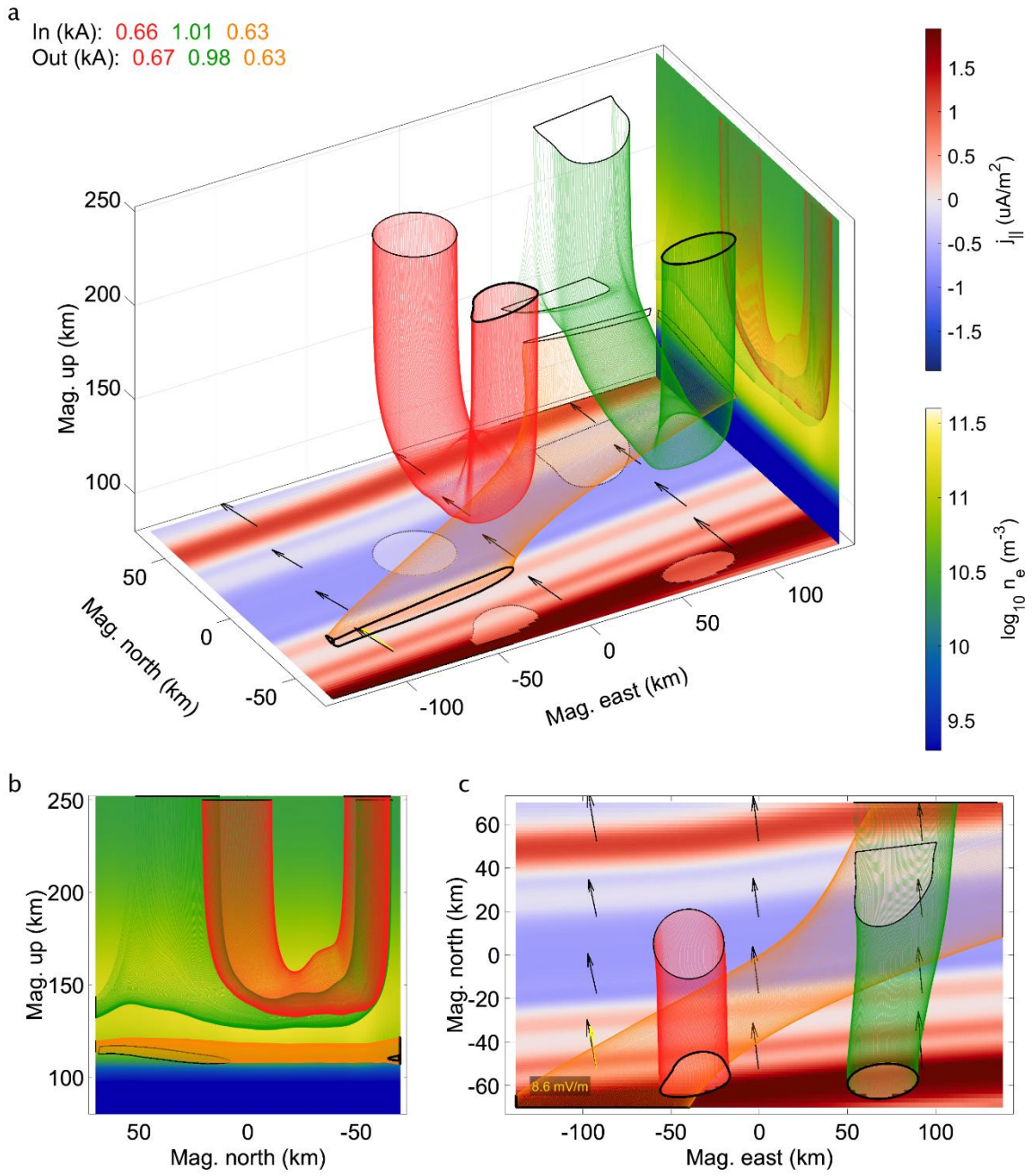

Figure S10. Simulations IIa and VIIa (February 12, 10:22 UT). Combination: SD-AM-xC. Tube set: 1. For plot details, see Section 2.8. Data sources found in respective comparison figures and the Open Research Section.

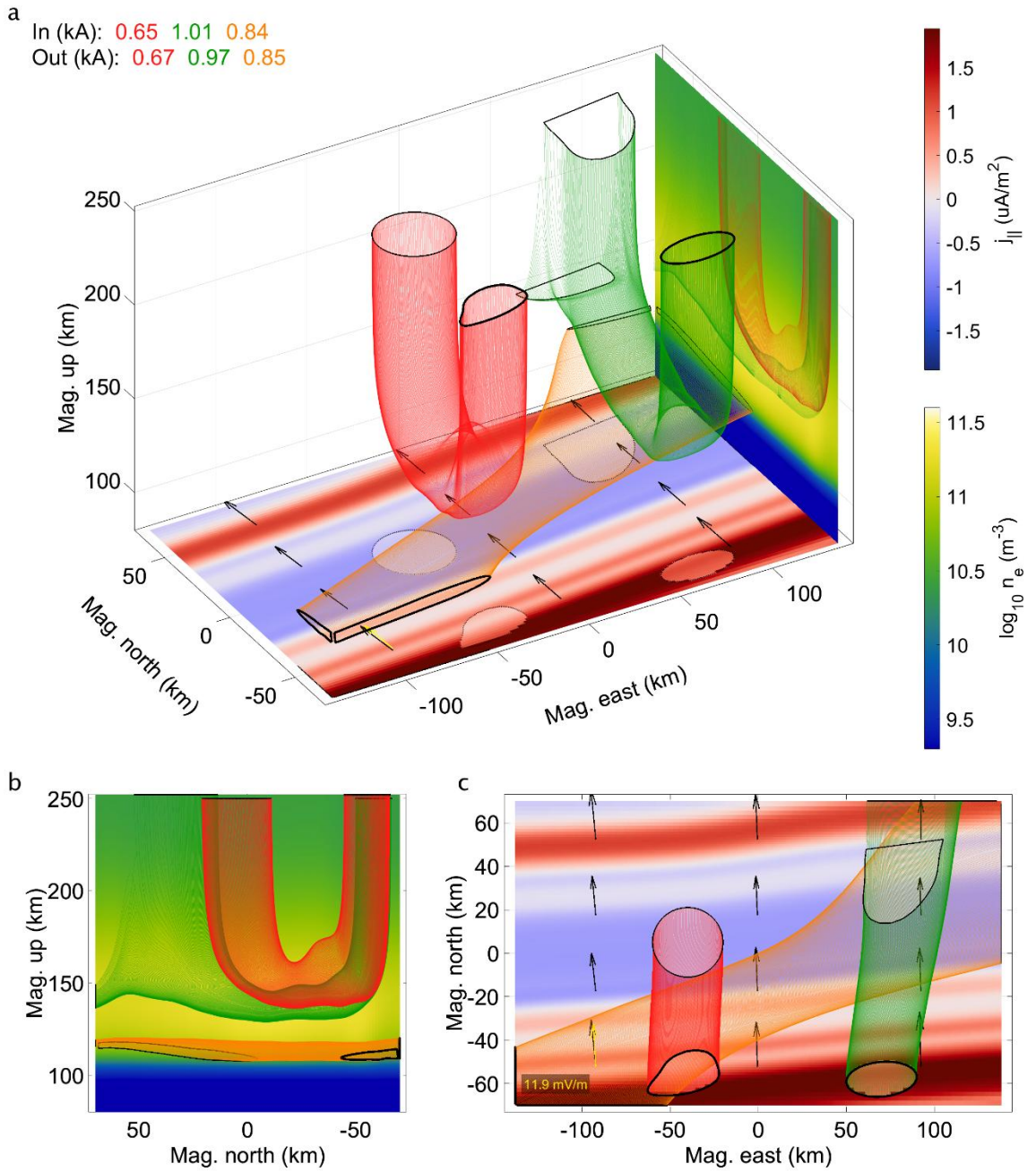

Figure S11. Simulation IIb (February 12, 10:22 UT). Combination: PF-AM-xC. Tube set: 1. For plot details, see Section 2.8. Data sources found in respective comparison figures and the Open Research Section.

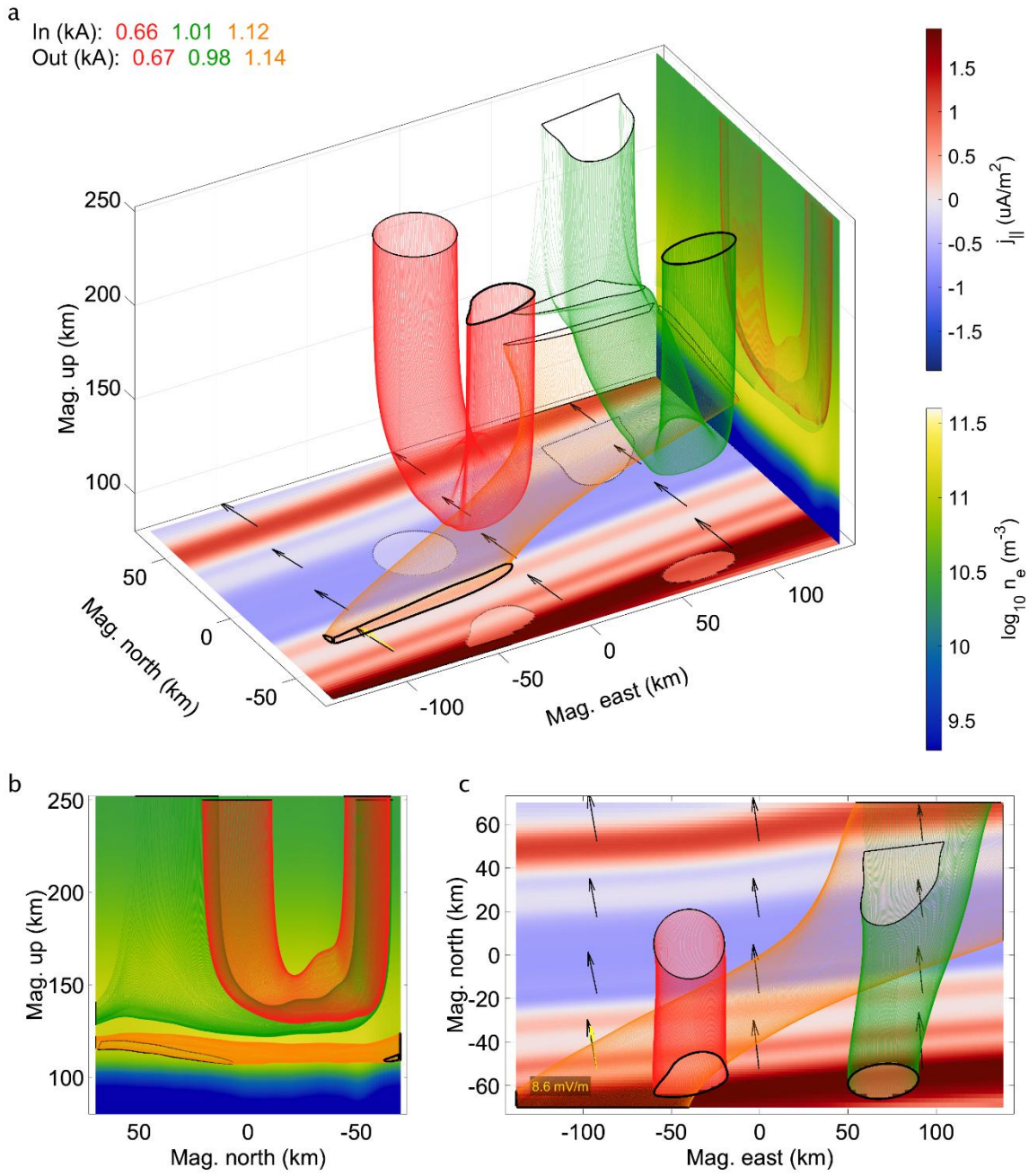

Figure S12. Simulation VIIb (February 12, 10:22 UT). Combination: SD-UM-xC. Tube set: 1. For plot details, see Section 2.8. Data sources found in respective comparison figures and the Open Research Section.

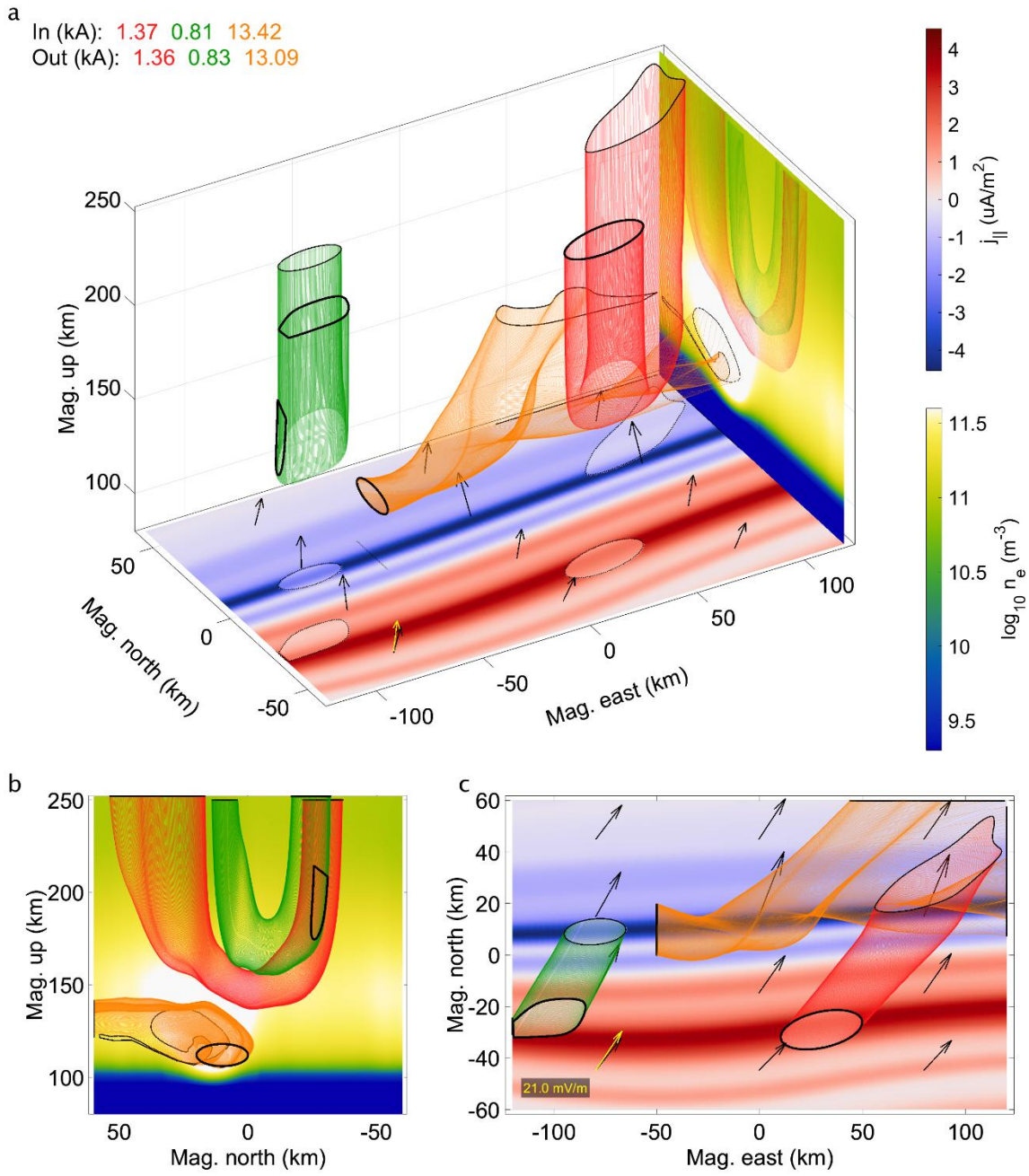

Figure S13. Simulations IIIa and VIIIa (March 4, 7:30 UT). Combination: SD-AM-xC. Tube set: 1. For plot details, see Section 2.8. Data sources found in respective comparison figures and the Open Research Section.

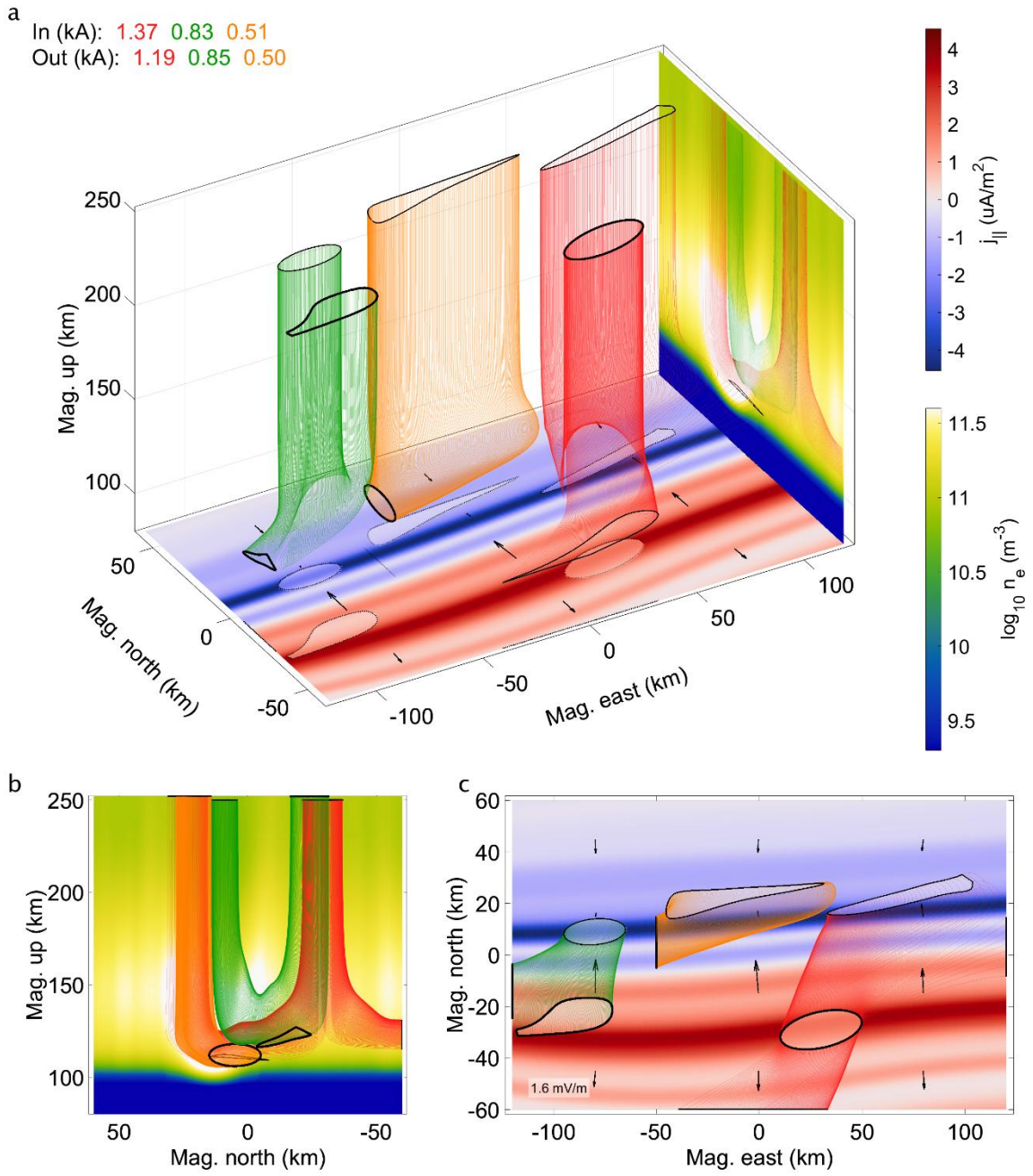

Figure S14. Simulation IIIb (March 4, 7:30 UT). Combination: NB-AM-xC. Tube set: 1. For plot details, see Section 2.8. Data sources found in respective comparison figures and the Open Research Section.

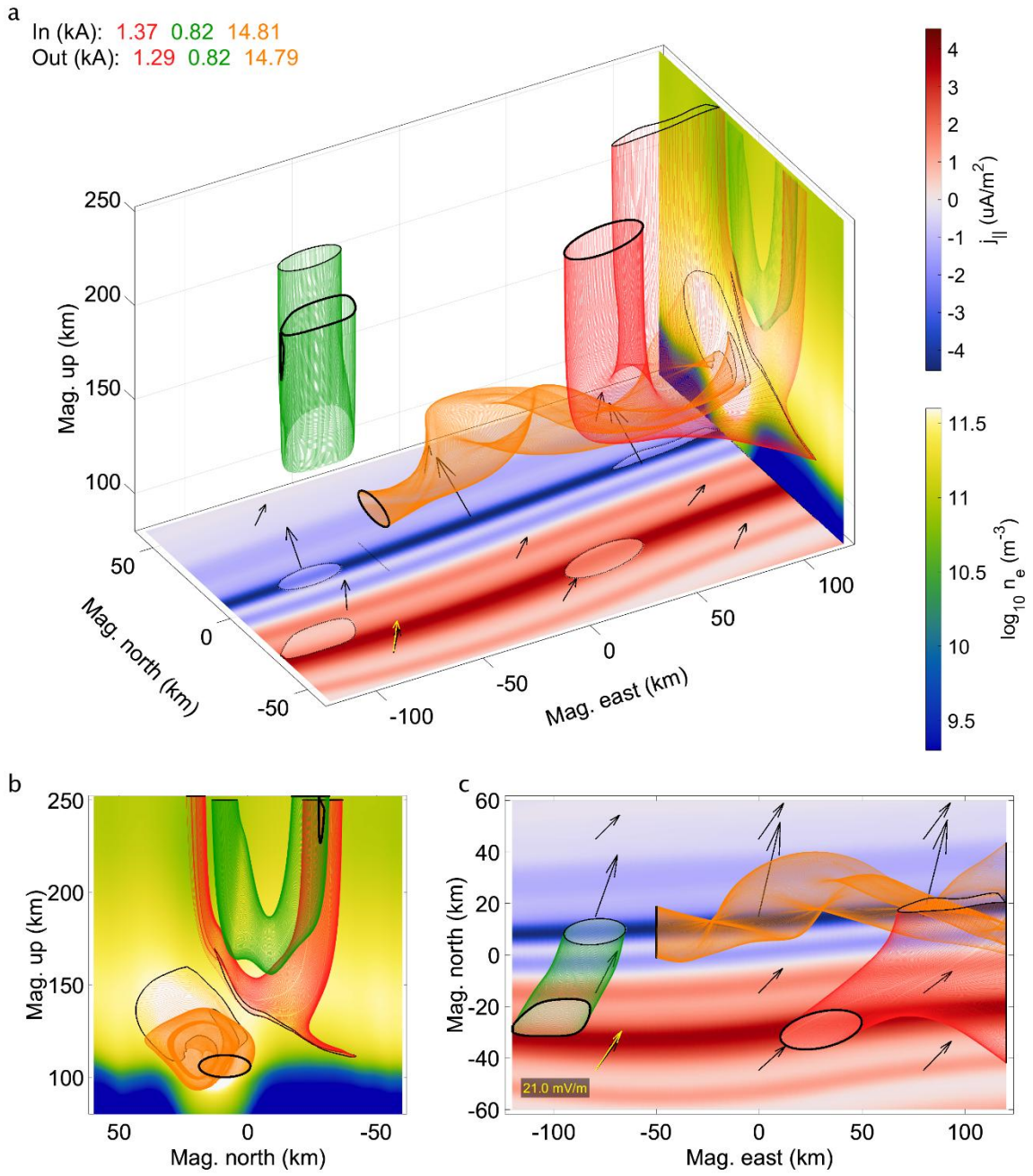

Figure S15. Simulation VIIIb (March 4, 7:30 UT). Combination: SD-UM-xC. Tube set: 1. For plot details, see Section 2.8. Data sources found in respective comparison figures and the Open Research Section.

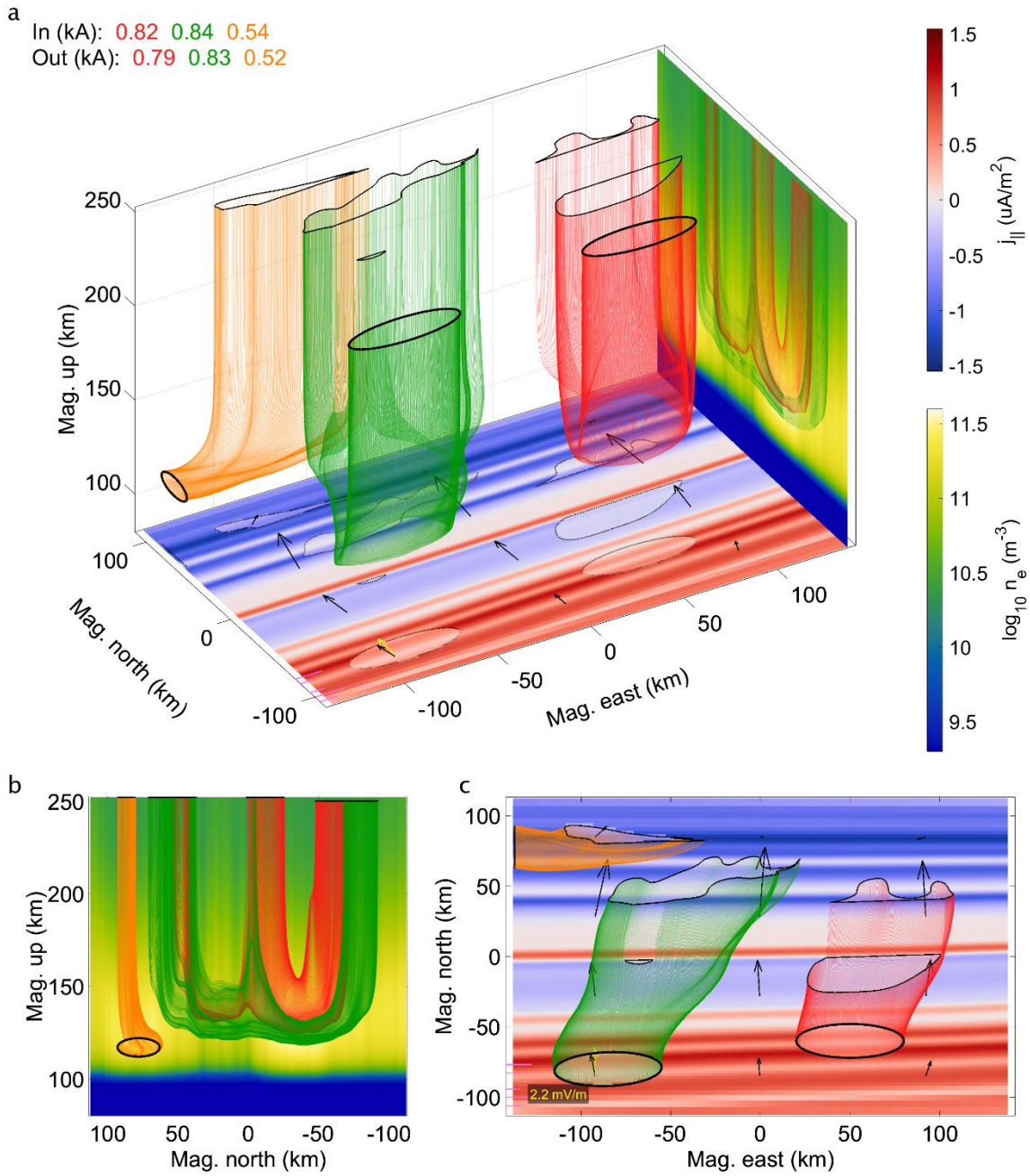

Figure S16. Simulation IXa (March 4, 10:14 UT). Combination: SD-AM-xB. Tube set: 1. For plot details, see Section 2.8. Data sources found in respective comparison figures and the Open Research Section.

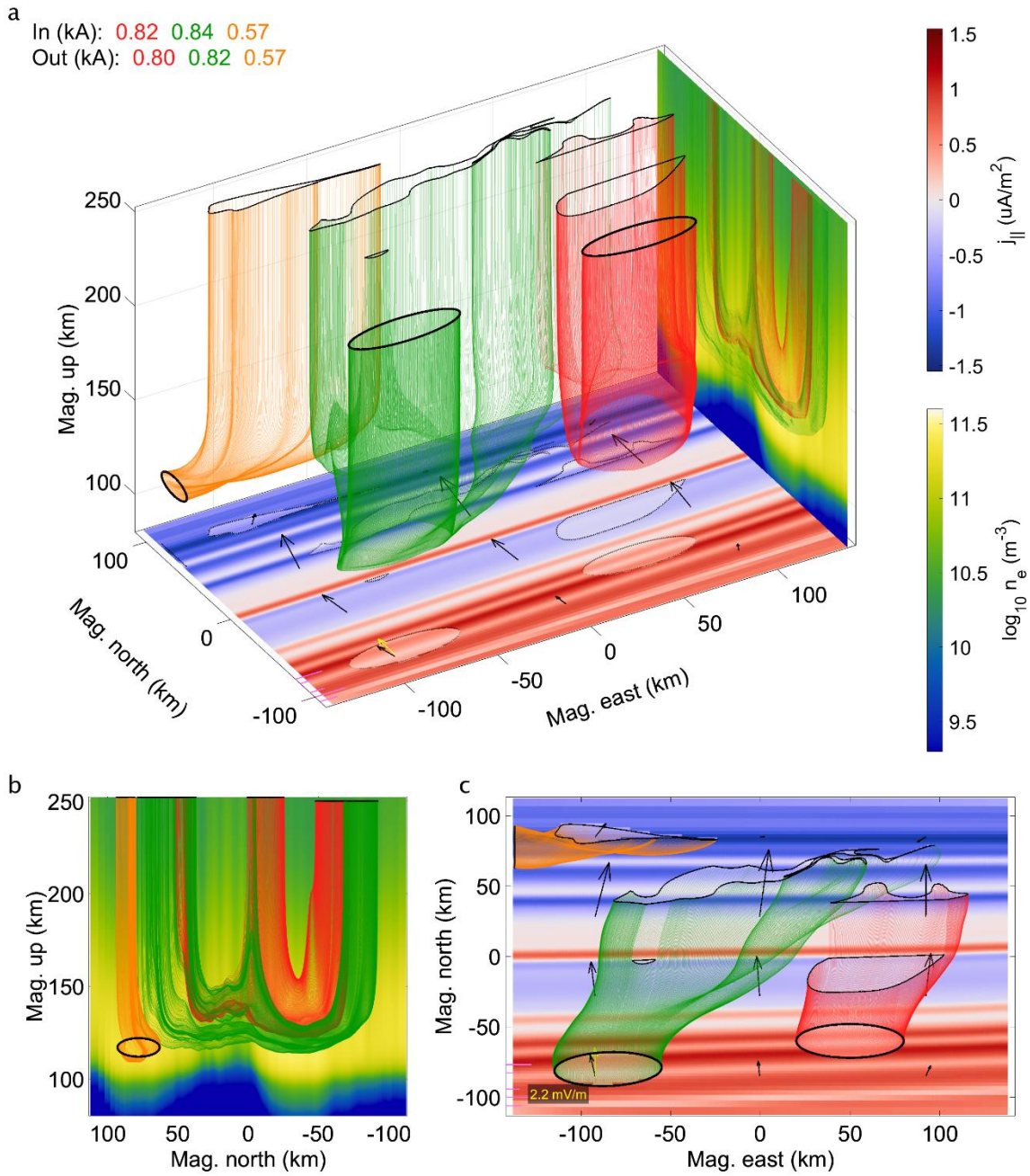

Figure S17. Simulation IXb (March 4, 10:14 UT). Combination: SD-UM-xB. Tube set: 1. For plot details, see Section 2.8. Data sources found in respective comparison figures and the Open Research Section.

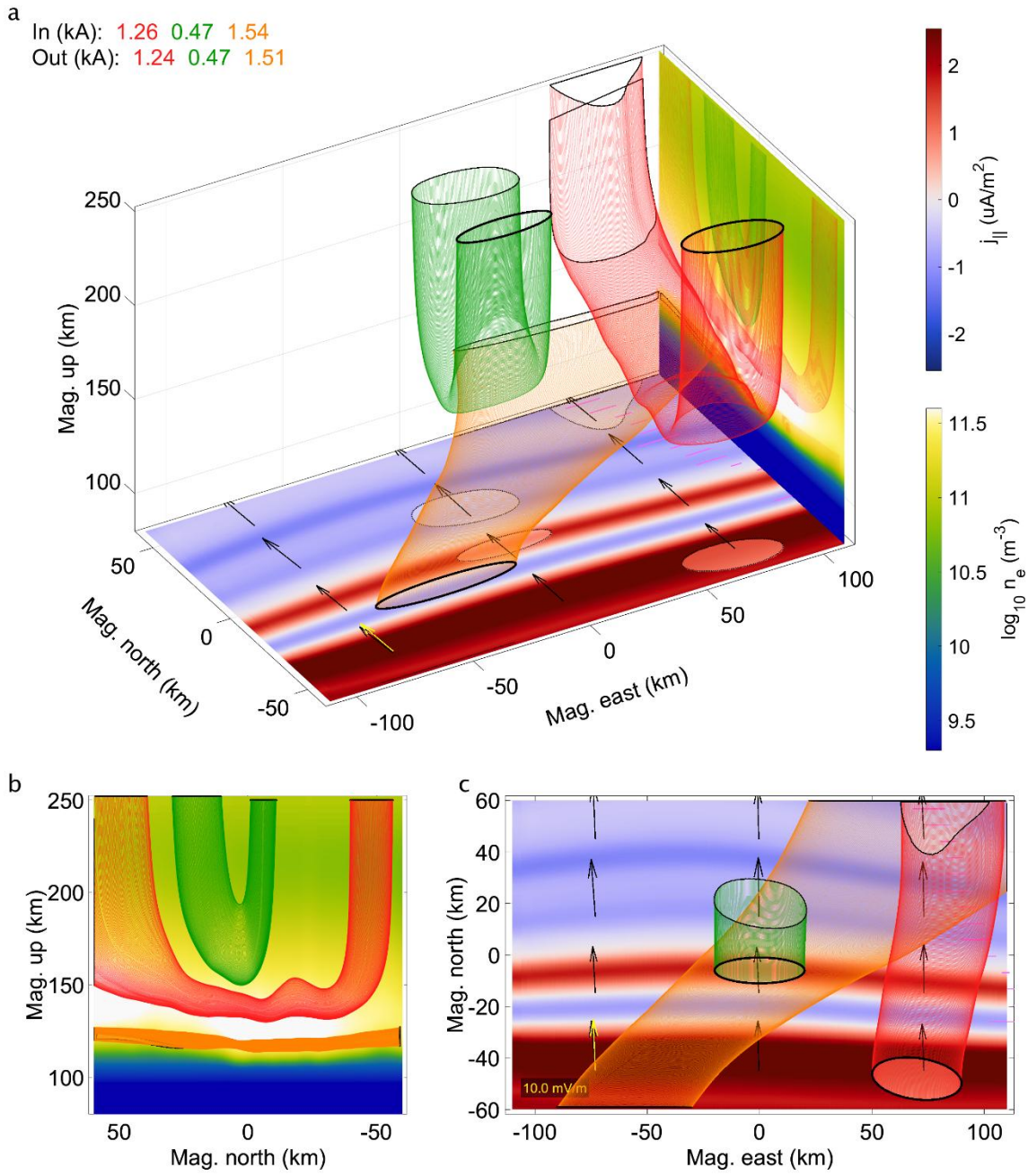

Figure S18. Simulations IVa and XIa (March 14, 6:49 UT). Combination: SD-AM-AC. Tube set: 1. For plot details, see Section 2.8. Data sources found in respective comparison figures and the Open Research Section.

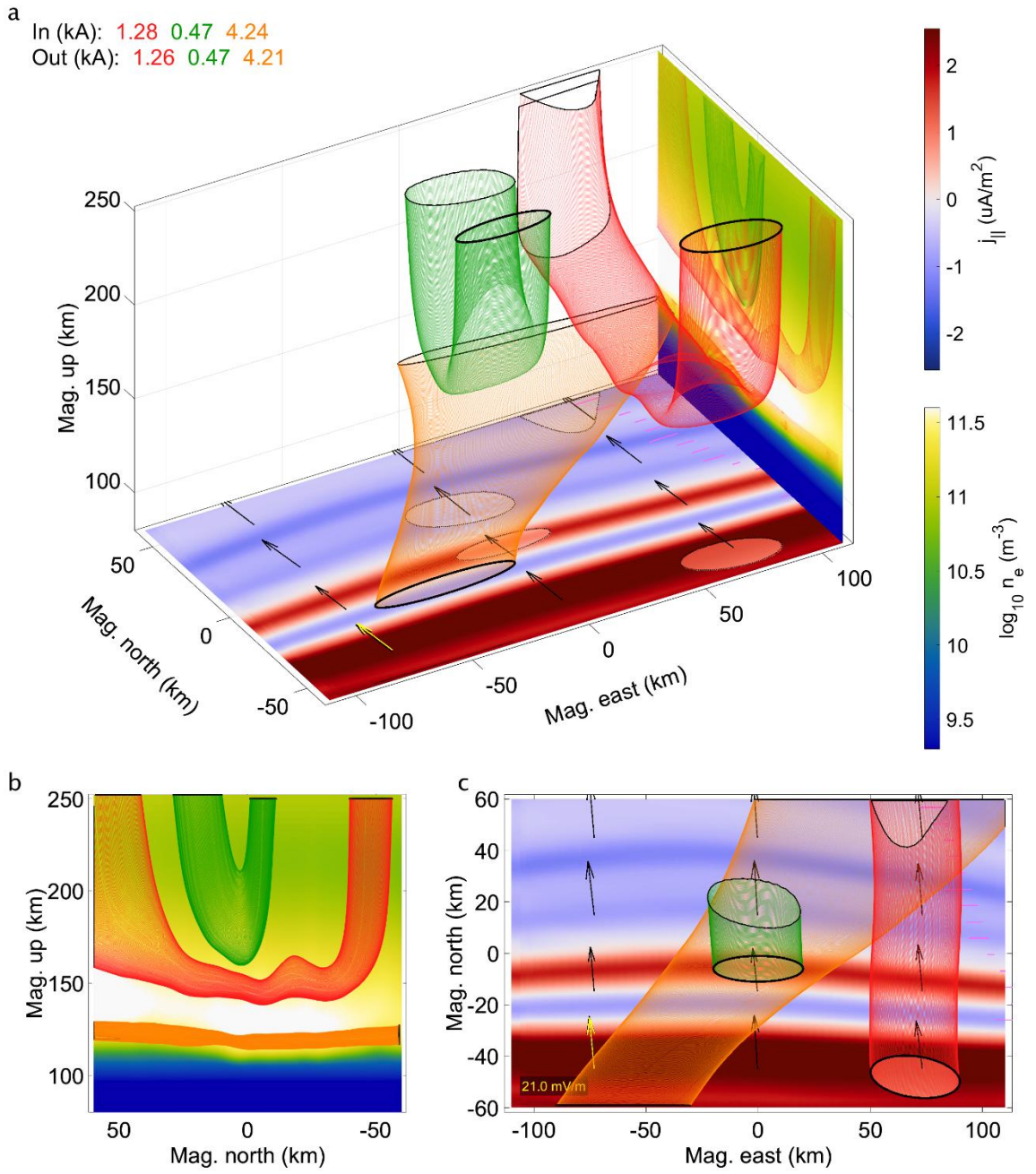

Figure S19. Simulation IVb (March 14, 6:49 UT). Combination: PF-AM-AC. Tube set: 1. For plot details, see Section 2.8. Data sources found in respective comparison figures and the Open Research Section.

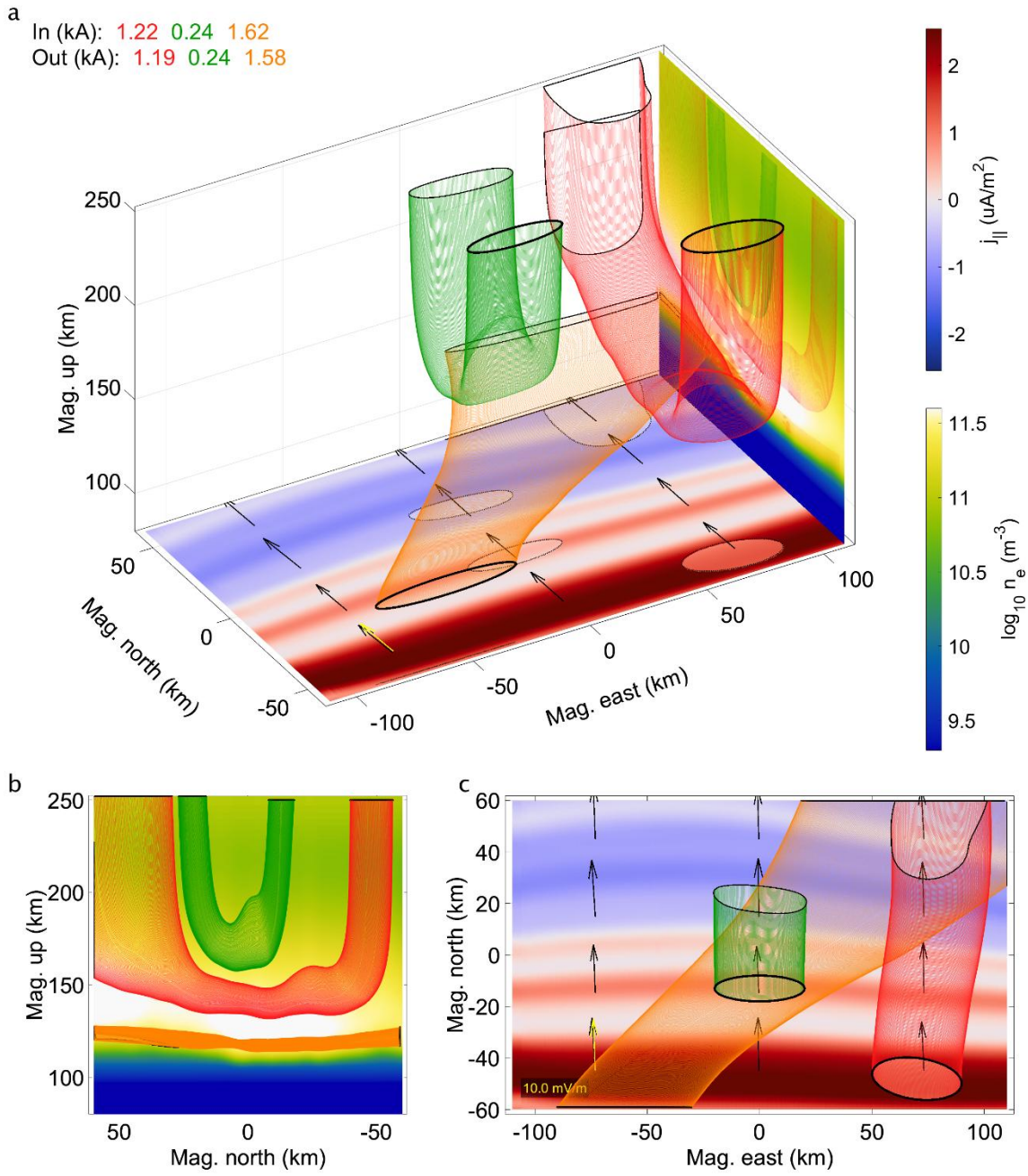

Figure S20. Simulation XIb (March 14, 6:49 UT). Combination: SD-AM-xA. Tube set: 1. For plot details, see Section 2.8. Data sources found in respective comparison figures and the Open Research Section.

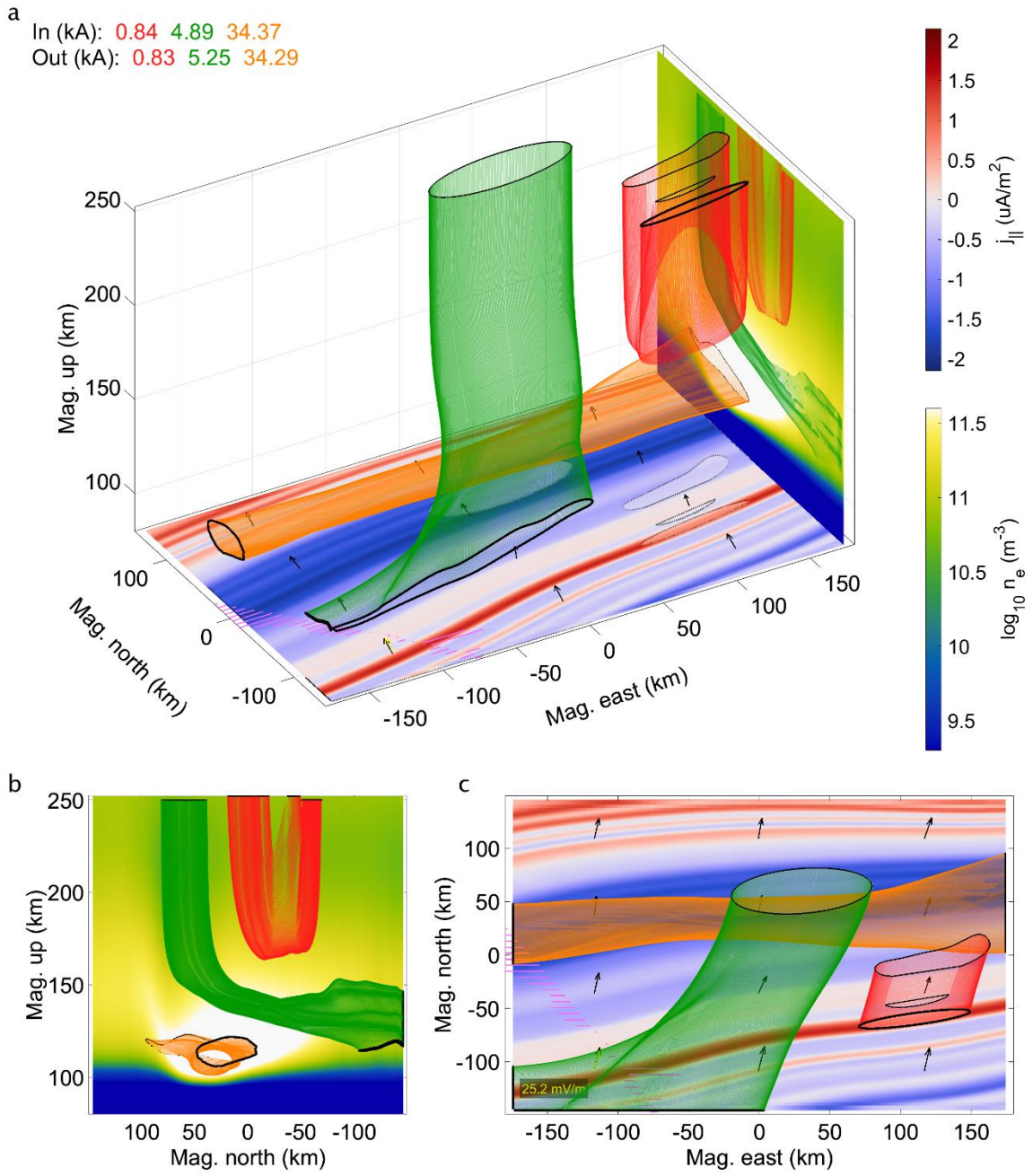

Figure S21. Simulation Va (March 19, 8:23 UT). Combination: SD-AM-xB. Tube set: 1. For plot details, see Section 2.8. Data sources found in respective comparison figures and the Open Research Section.

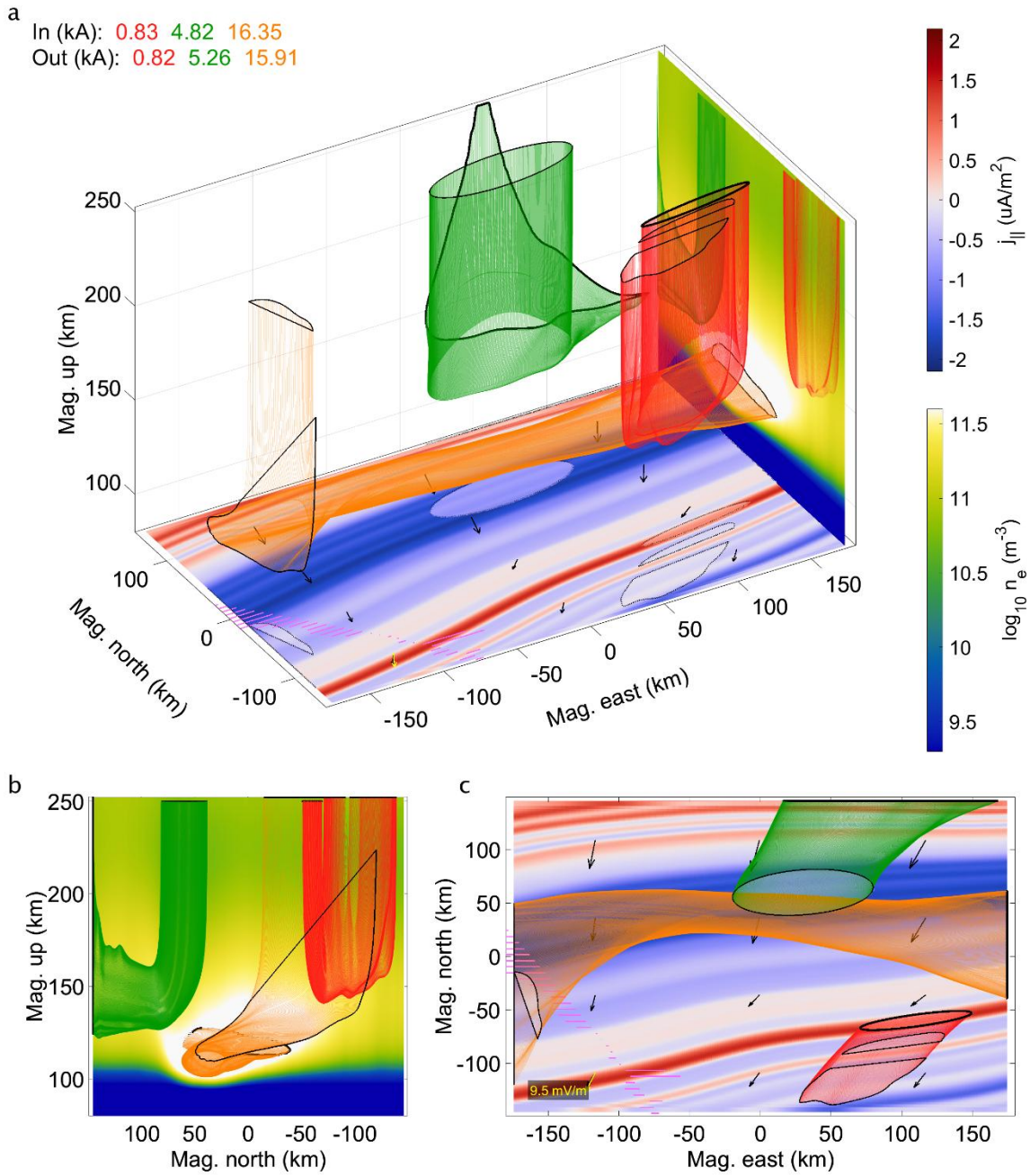

Figure S22. Simulation Vb (March 19, 8:23 UT). Combination: PF-AM-xB. Tube set: 1. For plot details, see Section 2.8. Data sources found in respective comparison figures and the Open Research Section.

Movie M1. Rotating view of Simulations Ia, VIa, and Xa (February 10, 9:51 UT). Combination: SD-AM-AC. Tube set: 1. For plot details, see Section 2.8. Data sources found in respective comparison figures and the Open Research Section.